Journal of Materials Chemistry A

Robust redox-reversible perovskite type steam electrolyser electrode decorated with in-situ exsolved metallic nanoparticles

Journal:	*Journal of Materials Chemistry A*
Manuscript ID	TA-ART-06-2019-006309.R2
Article Type:	Paper
Date Submitted by the Author:	12-Sep-2019
Complete List of Authors:	Liu, Tong; Wuhan University, School of Power and Mechanical Engineering Zhao, Yiqian; Wuhan University Zhang, Xiaoyu; Wuhan University Zhang, Hong; Wuhan University Jiang, Guang; Harbin Institute of Technology Zhao, Wen; Wuhan University Guo, Jiayi; Wuhan University Chen, Fanglin; University of South Carolina, Mechanical Engineering Yan, Mufu; Harbin Institute of Technology, School of Materials Science and Engineering Zhang, Yanxiang; Harbin Institute of Technology, School of Materials Science and Engineering Wang, Yao; Wuhan University,

Journal Name

ARTICLE

Robust redox-reversible perovskite type steam electrolyser electrode decorated with in-situ exsolved metallic nanoparticles

Received 00th January 20xx,
Accepted 00th January 20xx

DOI: 10.1039/x0xx00000x

www.rsc.org/

Tong Liu,[ab] Yiqian Zhao,[a] Xiaoyu Zhang,[a] Hong Zhang,[a] Guang Jiang,[c] Wen Zhao,[a] Jiayi Guo,[d] Fanglin Chen,[e] Mufu Yan,[c] Yanxiang Zhang,[*c] and Yao Wang[*ab]

Redox stabilities of the hydrogen electrode with *in-situ* exsolved Fe-Ni nanoparticles from $Sr_2Fe_{1.4}Ni_{0.1}Mo_{0.5}O_{6-\delta}$ (SFMNi) perovskite are studied by analyzing the evolution of the phase composition and morphology during the redox cycles. It is found that certain amount of the exsolved nanoparticles have been oxidized to transition metal oxide (Ni,Fe)O instead of reincorporating to the parent perovskite lattice upon re-oxidizing at 800 °C in air. However, the (Ni,Fe)O secondary phases show no adverse effect on the subsequent reduction treatment. The redox reversibility mechanism is explained by the regular-solution model. The electrodes are almost fully recovered in the reducing atmosphere, and the symmetrical cells measured in 9.7%H_2-3%H_2O-87.3%N_2 condition show stable specific area polarization resistance of around 1.93 Ωcm² at 800 °C during 13 redox cycles. Single cells using the Ni-Fe nanoparticle structured electrode exhibit a stable electrode polarization resistance of about 0.598 Ωcm² at 800 °C under open circuit voltage condition and a steady electrolysis current density of about -653 mAcm^{-2} at 1.5V during the steam electrolysis process upon 5 redox cycles. These results indicate that SFMNi material is a very promising electrode candidate for steam electrolysis application with robust redox reversibility.

1. Introduction

Solid oxide cell (SOC) is expected to go through a number of redox cycles during operation. The-state-of-the-art Ni-based cermet electrode, formed by reducing NiO to metallic Ni upon the operation of the SOC, has been proven to be an excellent catalyst for hydrogen (H_2) oxidation or water (H_2O) splitting reaction[1-9]. However, in case of unexpected interruption of fuel supply, gas sealing failure, or high fuel utilization in the fuel cell mode, Ni is re-oxidized to NiO, resulting in a substantial volume expansion and catalyst deactivation, leading to a significant microstructural change or electrochemical performance degradation[10-14]. For instance, Sarantaridis *et al.* investigated the changes in physical and mechanical properties of Ni-YSZ composite electrode caused by redox cycling, and found that the cermet had a significant expansion during an interrupted oxidation, which was not reversible in the subsequent reduction, resulting in a residual strain of 0.55~0.8% after the first redox cycle[12]. Kim *et al.* also studied the redox cycling stability of the Ni-YSZ composite electrode, which showed a reduction of electrical conductivity by 47% from 1200 to 600 Scm^{-1} over 20 redox cycles at 800 °C[13]. Fouquet *et al.* reported the electrolyte-supported cell using Ni-8YSZ as the anode showed an increase of the polarization resistance up to 18% after three redox cycles[14]. These previously reported results demonstrate that the traditional Ni-based cermet electrodes show low tolerance against redox cycling. Therefore, it is critical to increase the cell redox stability to accelerate the commercialization of SOC technology by improving the electrode tolerance or developing novel electrode with robust redox capability.

Recently, perovskite type oxides (ABO_3) have been intensively explored as alternatives to Ni-based cermet electrodes due to their stable phase structure in a wide range of oxygen partial pressure and flexible substitution of the B-site elements to alter the electrode performance functionality. Intensive studies have showed that easily reductive transition metals such as Ni and Co could be doped to the B-site of ABO_3 perovskite lattice during the sample preparation process in the oxidizing condition and then exsolved to the surface as metallic nanoparticles during the SOC operation in the subsequent reducing condition[15-24]. These in-situ exsolved nanoparticles are strongly pinned to the parent perovskite type oxides to form a composite electrode with a unique nano-particle socketed interface, and the exsolved metallic nanoparticles could significantly enhance the catalytic activity of the electrode, while the unique nanoparticle socketed interface could result in a robust resistance to nanoparticle agglomeration and coking when operated on carbonous fuels in the fuel cell mode[16, 23-27]. Moreover, it is reported that the metallic nanoparticles are feasible to be redox re-generative by incorporating into the parent perovskite type oxide under the oxidizing condition and exsolving again after switching back to the reducing atmosphere[6, 24, 28-33]. In

[a] *Key Laboratory of Hydraulic Machinery Transients (Wuhan University), Ministry of Education, School of Power and Mechanical Engineering, Wuhan University, Wuhan, Hubei 430072, China*
[b] *Suzhou Institute of Wuhan University, Suzhou, Jiangsu 215123, China*
[c] *National Key Laboratory for Precision Hot Processing of Metals, School of Materials Science and Engineering, Harbin Institute of Technology, Harbin, Heilongjiang 150001, China*
[d] *School of Urban Design, Wuhan University, Wuhan, Hubei 430026, China*
[e] *Department of Mechanical Engineering, University of South Carolina, Columbia, SC 29208, USA*
* Email: pmewy@whu.edu.cn (Y. Wang), hitzhang@hit.edu.cn (Y. Zhang)
† Footnotes relating to the title and/or authors should appear here.
Electronic Supplementary Information (ESI) available: [Experimental setup and electrochemical performance for symmetrical cells and single cells, and XPS, elemental maps, electrical conductivities, SEM images of SFMNi based samples.]. See DOI: 10.1039/x0xx00000x

addition, the re-generation efficiency of the nanoparticles is strongly related to the redox properties of the perovskite oxide. For instance, Lai *et al.* have studied the temperature effect on the evolution of Co-Fe nanoparticles exsolved from $La_{0.3}Sr_{0.7}Cr_{0.3}Fe_{0.6}Co_{0.1}O_{3-\delta}$ perovskite, and it was determined that the transition metals could be completely reincorporated into the perovskite lattice after re-oxidation at 800 °C, while partial nanoparticles remaining on the surface had been oxidized to $(Co,Fe)_3O_4$ at 700 °C [28, 29]. Yang *et al.* have reported the evolution of $SrFe_{0.85}Ti_{0.1}Ni_{0.05}O_{3-\delta}$ electrode during the redox process, and found that metallic Ni nanoparticles were exsolved to the surface by exposing to the 10%H_2-90%Ar atmosphere at 600 °C. After a subsequent re-oxidation at the same temperature for 10 min, metallic Ni was oxidized to NiO instead of incorporation to the perovskite lattice[34]. Zhu *et al.* have treated $Sr_2Fe_{1.3}Ni_{0.2}Mo_{0.5}O_{3-\delta}$ powders under three different atmospheres of H_2, 5%H_2/Ar and Ar to generate oxygen vacancies and exsolved metallic nanoparticles. Fe-Ni alloy was only observed in 5%H_2/Ar and H_2 atmospheres and the reduced SFMNi in 5%H_2/Ar showed the highest oxygen evolution reaction activity [35].

In recent years, $Sr_2Fe_{2-x-y}Ni_xMo_yO_{6-\delta}$ perovskite materials have been intensively explored as alternative hydrogen electrode for SOC application because of their excellent electrochemical performance induced by the *in-situ* exsolved Ni-Fe alloy nanoparticles from the parent perovskite oxide in the reducing atmosphere[17, 30, 35-41]. However, no comprehensive studies have been performed on the redox-reversibility of these materials, which is significant for the recovery of *in-situ* exsolved metallic nanoparticles. In this work, $Sr_2Fe_{1.5}Mo_{0.5}O_{6-\delta}$ is used as the parent perovskite oxide, and Ni is introduced to partially substitute Fe on the B-site to obtain $Sr_2Fe_{1.4}Ni_{0.1}Mo_{0.5}O_{6-\delta}$ (SFMNi), which can *in-situ* exsolve metallic Ni-Fe nanoparticles to form Ni-Fe@SFMNi composite nano-electrode under the SOC working condition, serving as the cathode for steam electrolysis application. The reversibility of exsolved nanoparticles is examined by the phase characterization and morphology observation during the redox cycling, and explained by the regular-solution model. In addition, symmetrical cells with a cell configuration of SFMNi/ $La_{0.5}Ce_{0.5}O_{1.75}$ (LDC) / $La_{0.80}Sr_{0.20}Ga_{0.80}Mg_{0.20}O_{3-\delta}$ (LSGM) / LDC / SFMNi are measured in 13 redox cycles to determine the evolution of the electrode polarization resistance (Rp). Finally, the redox cycling property of the single cells using Fe-Ni@SFMNi based nano-electrode for the hydrogen production via steam electrolysis process is also evaluated.

2. Experimental

2.1 Fabrication of single cells

The electrolyte-supported solid oxide electrolysis cells with a cell configuration of SFMNi-$Ce_{0.8}Sm_{0.2}O_{1.9}$(SDC)/LDC/LSGM/ $Ce_{0.9}Gd_{0.1}O_{1.95}$(GDC)-$(La_{0.6}Sr_{0.4})_{0.95}Co_{0.2}Fe_{0.8}O_{3-\delta}$(LSCF) are fabricated to perform the steam electrolysis process for hydrogen production. The LSGM electrolyte powders and LSCF-GDC anode ink with a weight ratio of 50:50 were purchased from FuelCellMaterials Inc., while the SFMNi powders, SDC powders and LDC interlayer powders were synthesized using the citric-assisted combustion method[42-44]. The dense LSGM electrolyte disk was prepared by pressing the powders into pellet and sintered at 1400 °C for 5 hours. The LDC interlayer was prepared by dropping the slurry on one side of the dense electrolyte substrate and sintered at 1250 °C for 5 hours. The SFMNi-SDC cathode ink was prepared by mixing the SFMNi powders and SDC powders in a weight ratio of 50:50 with an organic binder, and then printed on the LDC side while the LSCF-GDC anode ink was printed on the other LSGM surface. These two inks were then subsequently co-sintered at 1050 °C for 5 hours. The gold (Au) paste was used as the current collector. The active anode area was 0.33 cm^2. The single cells were measured on a home-made testing system, which was schematically shown in Figure S1. During the operation, the GDC-LSCF anode and the SFMNi-SDC cathode were exposed to atmospheric air and 26%H_2O-74%H_2 atmosphere, respectively. The humidified fuel was obtained by passing H_2 through a water bubbler, which was heated to certain temperature based on the saturation vapor pressure. The exact practical water pressure was monitored by an on-line humidity sensor (HMP 337, Vaisala). Electrochemical performance is measured using a Versa STAT 3-400 test system (Princeton Applied Research). The current density–cell voltage (*i–V)* curves were recorded in the voltage range from 0 to 1.5 V at a sweeping speed of 0.03 V s^{-1}. Electrochemical impedance spectra (EIS) were recorded in the frequency range of 0.01–1 MHz with a voltage amplitude of 30 mV. Symmetrical cells with a configuration of SFMNi/LDC/LSGM/LDC/SFMNi were fabricated to study the polarization resistance evolution of Ni-Fe nanoparticles structured SFMNi electrode during the redox cycling process. The cells were fabricated similarly as that of the single cells. The electrochemical performance of symmetric cells was performed on a home-made testing system, as schematically shown in Figure S2. To investigate the redox tolerance and self-regeneration property of SFMNi based electrode, symmetrical cells were measured by using EIS with the voltage amplitude of 30 mV in the frequency range from 10^6 to 10^{-2} Hz in a number of redox cycles, which were performed by switching the atmosphere from air to N_2 then to 9.7%H_2-3%H_2O-87.3%N_2 and vice versa.

A rectangular SFMNi bar sample with a size of 40 × 6 × 1 mm^3 mm was fabricated by uniaxially pressed at 300 MPa, and followed by sintering at 1300 °C for 5 h in air for electrical condutivity test via a multimeter (Keithley model 2001) by using the four-probe method. The morphology of the symmetrical cells as well as the morphology evolution of the fuel electrode are measured via a scanning electron microscopy (SEM, Tescan MIRA 3 and Zeiss GeminiSEM 500). To test the phase composition, morphology and structure evolution of SFMNi material during the redox process, the as-prepared SFMNi powders as well as SFMNi disk samples were first reduced in humidified hydrogen (3% H_2O) at 800 °C with a dwell time of 10 h, and then treated in atmospheric air at 800 °C for 10 h, and subsequently re-reduced at 800 °C for 10 h in humidified hydrogen (3% H_2O). X-ray diffraction (XRD) data of these powders were collected in a PANalytical Xpert Pro using Cu Kα radiation at a scan rate of 5 ° min^{-1} with 0.02 ° step size in the 2θ range of 20-80 °. X-ray photoelectron spectroscopy (XPS) of these materials was recorded in an ESCALAB250Xi (Thermo Fisher Scientific) using Al Kα X-ray source, and the binding energies were calculated with respect to C 1s at 285 eV and were measured with a precision of 0.2 eV. The detailed microstructure observation as well as the elemental mapping results of these powders were performed using a FEI Tecnai G2 F20 S-TWIN FEG transmission electron microscopy (TEM).

3. Results and discussion

3.1. Phase Composition and Microstructure Evolution

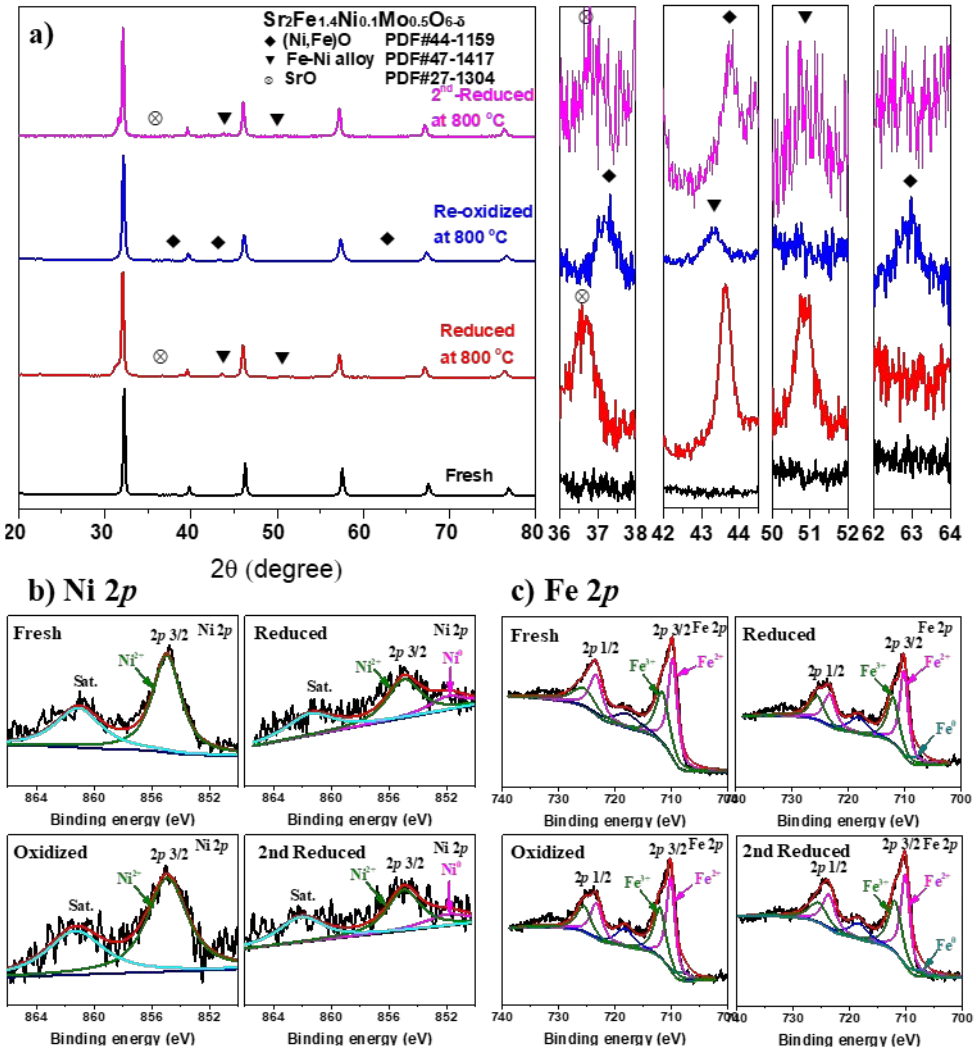

Figure 1 a) XRD patterns, and b-c) XPS of core level regions of SFMNi powders during a redox process, b) Ni 2*p*, and c) Fe 2*p*.

.

Figure 1a shows XRD patterns of SFMNi based powders during the redox process. It can be seen that the pristine SFMNi powders calcined at 1050 °C show a single cubic perovskite structure (PDF# 34-0638) with no impurity phases, indicating that Ni ions (Ni^{2+}: 0.072 nm, Ni^{3+}: 0.062 nm) have been completely doped into the perovskite lattice due to the similar ion radii and valence properties to Fe ions (Fe^{2+}: 0.074 nm, Fe^{3+}: 0.064 nm). These powders are then reduced at 800 °C in 97%H_2-3%H_2O atmosphere for 10 hours, and the reduced SFMNi sample also presents predominately the same phase structure as the pristine one. However, three additional characteristic diffraction peaks at 36.5, 43.6 and 50.8 ° are detected, the peak with the lowest angle can be attributed to SrO (PDF #27-1304), while the other two peaks with laeger degrees are identified as taenite, a Fe-Ni alloy (PDF #47-1417). These two phases formed at rduced state are possibly ascribed to the partially decompostion of parent SFMNi oxide. The reduced SFMNi powders are then re-oxidized in air at 800 °C to examine the redox cycling stability, and it is found that another three peaks located at 37.3, 43.3 and 63.0 ° belonging to (Ni,Fe)O are observed instead of the characteristic peaks detected at 43.6 and 50.8 ° for Ni-Fe alloy. These results demonstrate that the exsolved metal particles has not been fully reincorporated to the parent perovskite lattice, and certain amount of the Ni-Fe alloy particles has been re-oxidized to the transition metal oxide ((Ni,Fe)O), which is similar to the result reported by Lai *et al* that *in-situ* exsolved Co-Fe alloy nanoparticles have been partially oxidized to $(Co,Fe)_3O_4$ instead of complete reincorporation into the $La_{0.3}Sr_{0.7}Cr_{0.3}Fe_{0.6}Co_{0.1}O_{3-\delta}$ perovskite[28, 29]. Moreover, after the 2nd reduction in the humidified hydrogen at 800 °C, the two characteristic diffraction peaks identified as Ni-Fe alloy at 43.6 and 50.8 ° emerged and the (Ni,Fe)O peaks disappered while the 2nd reduced SFMNi sample also shows the same structure as the 1st reduced one, implying that the Ni-Fe alloy nanoparticles decorated SFMNi materials can be re-generated during the redox operation.

The states of the elements of these SFMNi powders were identified by XPS measurement, and Figure 1b and 1c show the XPS spectra of core level regions of Ni 2*p* and Fe 2*p* of these SFMNi powders during

a redox process. Only one peak with the XPS binding energy of 855.0 eV for Ni^{2+} $2p_{3/2}$is observed for Ni element in fresh SFMNi powders, while a mixed valence state is detected for Fe element because the peaks centered at 712.1 and 710.1 eV are associated with Fe^{3+} $2p_{3/2}$ and Fe^{2+} $2p_{1/2}$, respectively. However, after reduction in humidified hydrogen (97%H_2-3%H_2O), both Ni^0 $2p_{3/2}$ (851.6 eV) and Fe^0 $2p_{3/2}$ (707.8 eV) peaks besides Ni^{2+} $2p_{3/2}$ and $Fe^{2+/3+}$ $2p_{3/2}$ are detected on the surface of reduced SFMNi powders (reduced sample), indicating that a part of Ni^{2+} and $Fe^{2+/3+}$ in the fresh SFMNi powders (fresh sample) have been reduced to metallic Ni and Fe, which is in agreement with the XRD results shown in Figure 1a[40]. It can also be found that both Ni^0 $2p_{3/2}$ and Fe^0 $2p_{3/2}$ peaks disappear after re-oxidizing the powders in air at 800 °C (oxidized sample), but can be re-generated by further switching the gas from air to humidified hydrogen (2^{nd} reduced sample). Meanwhile, the XPS spectra of O 1*s*, Mo 3*d*, and Sr 3*d* are also analyzed and shown in Figures S3-6. It is shown in Figure S4 that the average valence state of element Mo, which is mixed by Mo^{5+} and Mo^{6+}, is reduced after reduction or 2^{nd} reduction in the humidified hydrogen, but increased after re-oxidized in air. Figure S5 shows XPS of O1s of core level regions of SFMNi powders during a redox process, and the peak with the binding energy of 529.4 eV in Figure S5 is attributed to the lattice oxygen species (O^{2-} or O_{lat}), and the peak with a binding energy of 531.0 eV likely corresponds to reactive oxygen species (O_2^{2-}/O^-) [17, 35, 39], moreover, the ratio of reactive oxygen species (O_2^{2-}/O^-) to lattice oxygen species (O_{lat}) initially increases, then decreases , and finally re-increases during the redox process (Figure S5). Therefore, it can be seen that these XPS results well agree with the XRD results, confirming the redox reversibility of these SFMNi based materials.

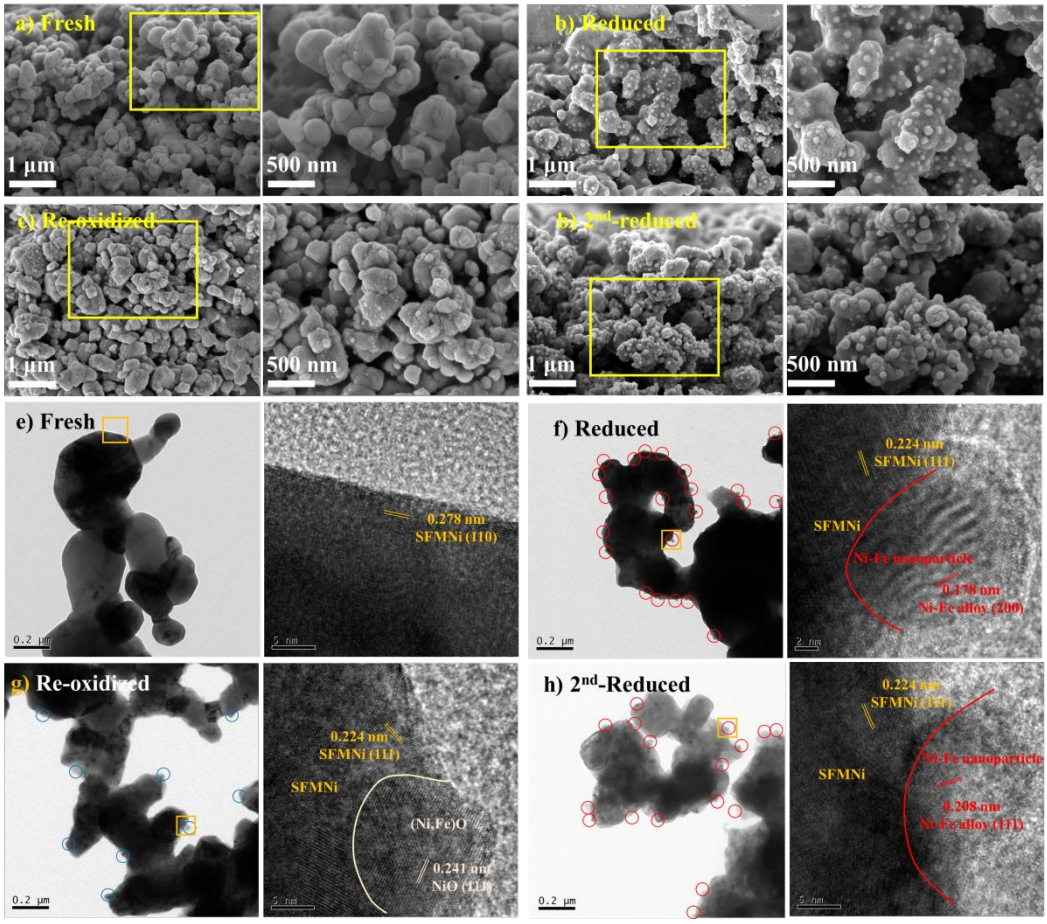

Figure 2 a-d) SEM images of the surface of the SFMNi hydrogen electrode samples, and e-h) TEM images of the SFMNi powders samples. a-e) Fresh sample, b-f) reduced sample prepared by treated in the humidified hydrogen atmosphere at 800 °C for 10 hours, c-g) Re-oxidized sample treated in air at 800 °C for 10 hours, and d-h) 2^{nd} reduced sample prepared by re-reducing the re-oxidizing sample in the humidified hydrogen atmosphere at 800 °C for 10 hours.

To further evaluate the redox reversibility of these SFMNi based materials, the morphology and structure evolution of these materials during the redox process has been investigated in detail by using SEM and TEM. Figure 2a-d shows the surface morphology of SFMNi hydrogen electrode samples during the redox operation. It can be seen from Figure 2a that after calcined at 1050 °C for 2 hours, the SFMNi hydrogen electrode sample is porous, and has a clean and smooth surface. After reduction of the SFMNi sample in 3%H_2O-97%H_2 atmosphere at 800 °C for 10 hours, a large number of nanoparticles, which have been identified as Fe-Ni alloy by XRD and XPS results, are *in-situ* exsolved from the perovskite parent as shown in Figure 2b[17, 36-38]. These metallic nanoparticles are strongly pinned into the perovskite substrate with a spherical shape and an average particle size of 60 nm, which are expected to serve as active

reaction sites for steam splitting reaction, thus effectively increasing the electrochemical performance of the electrolyzer as well as the hydrogen production rate. The redox properties of SFMNi material are further investigated by a subsequent re-oxidation treatment in a flowing air atmosphere for 10 hours, and the morphology shown in Figure 2c indicates that it does not completely revert to the fresh one. Most of the metal nanoparticles have been reincorporated back into the parent perovskite lattice, leaving dents in their original position. The surface of re-oxidized sample becomes very rough when compared with the fresh sample, and a few spherical nanoparticles remain on the surface of the porous hydrogen electrode, which are possibly oxidized to (Ni,Fe)O after re-oxidation at 800 °C for 10 hours, indicating that the reincorporation process is not complete due to the sluggish rate. Surprisingly, after re-reducing in humidified hydrogen, as shown in Figure 2d that a significant amount of nanoparticles are *in-situ* re-exsolved from and strongly pinned onto the parent perovskite type oxide. It should be pointed out that the preparation conditions have certain influence on the exsolution and reincorporation process, which are strongly associated with the morphology evolution during the redox operation and confirmed by the observed SEM images of porous SFMNi electrode and dense SFMNi pellet shown in Figure 2a-d and Figure S7, demonstrating that it is recommendable to use practical hydrogen electrode to check the reversible exsolution process during the redox operation instead of the sample prepared at other conditions. In addition, TEM images as well as the elemental mapping of these four powders are also collected to further identify the evolution of phase composition and morphology, as presented in Figure 2e-h and Figures S8-15, respectively. It can be seen from Figure 2e that only one lattice distance of around 0.278 nm has been revealed, which is consistent with that of the (110) plane of SFMNi crystalline structure (space group Pm3m), indicating that the fresh SFMNi powders calcined at 1050 °C for 5 h are single phase. After reduction, as presented in Figure 2f that a number of nano-size particles are exsolved from the parent oxide, and two typical lattice distances of around 0.224 and 0.178 nm have been clearly observed in the nanoparticle/parent oxide region, and the former is in agreement with the lattice distance of the (200) plane of SFMNi phase (space group Pm3m) determined by XRD results while the latter fits well with the lattice distance of the (111) plane of Ni-Fe alloy (Taenite, space group Fm3m). These results reveal that Ni-Fe alloy nanoparticle structured perovskite oxide has been successfully prepared via *in-situ* exsolution method in the reducing atmosphere, further confirmed by the elemental mappings measured by energy dispersive spectroscopy (EDS) (Figure S8-11). After re-oxidizing the reduced powders, some nanoparticles can still be detected, and the lattice distances of the parent oxide and the nanoparticles are measured to be 0.224 and 0.241 nm, respectively, which are concluded to be SFMNi perovskite oxide and (Ni,Fe)O by using XRD and XPS results. Meanwhile, Ni elemental enrichment region is observed from the elemental mapping images shown in Figure S12-13, indicating that the exsolved metal particles have not been fully reincorporated to the parent perovskite oxide, but partially re-oxidized to t (Ni,Fe)O. However, subsequent reduction of the re-oxidized SFMNi powders in humidified hydrogen, Ni-Fe nanoparticles decorated SFMNi powders without other phases are successfully regenerated (Figure 2h and Figure S14-15), which is also confirmed by XRD, XPS and SEM results. Consequently, analysis of the results from XRD, XPS, SEM, and TEM demonstrates that the as-prepared SFMNi materials can have excellent redox-reversibility through self-regeneration, offering a great promise to meet the redox stability requirement for practical SOC applications.

2.2. Self-Regeneration Mechanism

The self-regeneration ability of Ni-Fe alloy nanoparticles at the exposed grain surface of SFMNi matrix can be explained by a thermodynamic regular-solution model. According to the operating conditions, SFMNi perovskite can be treated as a solid solution system consisting of three phases - perovskite matrix (PM), environment (EN) and nanoparticles (NP, mainly Ni) and three components - stoichiometric perovskite (A), B-site dopant (B') and pores (P). The homogenous Gibbs free energy per molar of the solid solution can be expressed by regular-solution model (Equation (1)),

$$g = \sum_{i=\mathrm{A,B',P}} \left\{ [\mu_i^0 + (1-\eta^2)\mu_i^{\mathrm{seg}}] x_i + x_i RT \ln x_i \right\} + \sum_{i=\mathrm{A,B',P}} \sum_{j>i} x_i x_j L_{ij}(P_{\mathrm{O2}}) \quad (1)$$

where η is an order parameter representing the surface region, x_i,and x_j denote molar fractions of species i and j, respectively, $\mu_i^0 + (1-\eta^2)\mu_i^{\mathrm{seg}}$ denotes the standard chemical potential, R denotes gas constant, T denotes absolute temperature and $L_{ij}(P_{\mathrm{O2}})$ represents the implicit relationship between oxygen partial pressure (P_{O2}) and interaction energies between components i and j, which can be increased by decreasing P_{O2}. The thermodynamic basis of the reversible ex-solution can be explained by the reversible change in $L_{ij}(P_{\mathrm{O2}})$. In reducing atmosphere (a low P_{O2}), $L_{ij}(P_{\mathrm{O2}})$ is increased so that the spinodal region is expanded, leading to the exsolution of nanoparticles although the doping level is low. When the atmosphere is switched to be oxidizing (a high P_{O2}), $L_{ij}(P_{\mathrm{O2}})$ is decreased so that the spinodal region shrinkages or even be diminished. Therefore, the up-hill diffusion will turn to be a down-hill type. Thus, the exsolved particles can be re-incorporated into the matrix. The same model parameters are selected as the reference condition in our previous work[45]. The only difference is the decrease of $L_{ij}(P_{\mathrm{O2}})$ from 4.5 (corresponding to reduction) to 2.5 (corresponding to oxidation) at the 3×10^5th time step, to simulate a reduction-oxidation cycle. Figure 3 shows the snap-shoots of the exsolution at t^*=0.5×10^5, 2.5×10^5 (Figure 3a-b) and the redissolution at t^*=4×10^5 (Figure 3c). It is interesting to note that the predicted results of the phase-field model are consistent with the experimental observations. Thus, the thermodynamics basis for the reversible exsolution can be interpreted by the reversible shift of the free energy surface (Equation (1)) between spinodal type at reducing atmosphere (or high L_{ij}) and spinodal-free type at oxidizing atmosphere (or low L_{ij}).

From analysis of the XRD patterns, XPS spectra, SEM images, TEM images, elemental mappings as well as the results calculated by regular-solution model, a self-regeneration mechanism for perovskite oxide SFMNi based materials is proposed and schematically illustrated in Scheme 1. Ni-Fe alloy nanoparticles are *in-situ* exsolved from the pristine SFMNi parent oxide by reducing the materials in humidified hydrogen (3% H_2O), and strongly pinned to the parent oxide. After re-oxidizing the reduced sample in air, these Ni-Fe nanoparticles do not completely reincorporate to the pristine one, but partially form wedge-shape/cuneiform (Ni,Fe)O particles at the grain boundary area of the parent oxide. However, re-switching

the operating atmosphere from air to humidified hydrogen, Ni-Fe alloy nanoparticles pinned into SFMNi are re-generated..

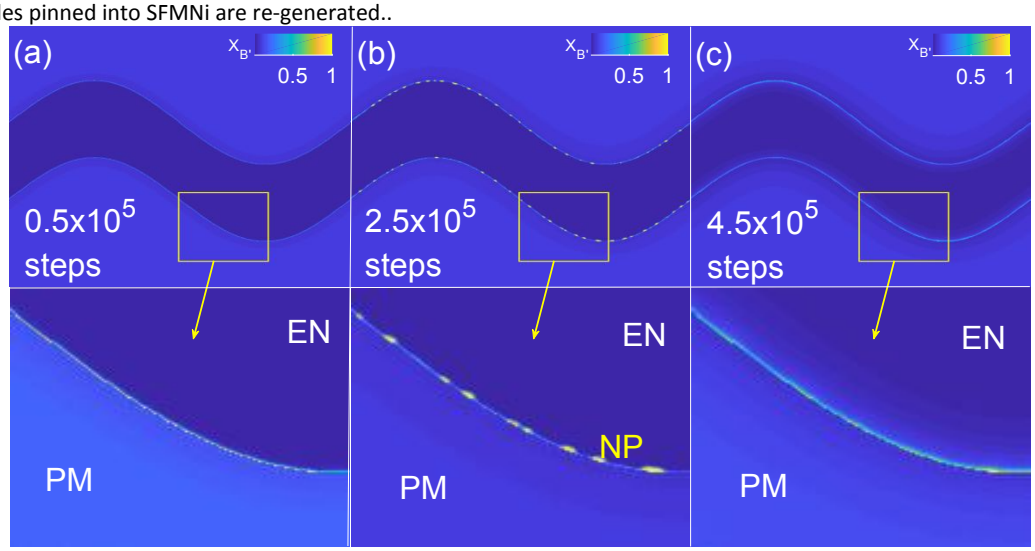

Figure 3. Contour plots of the molar fraction of Ni ($X_{B'}$) derived from the phase field model with dimensionless model parameters. The exsolution-redissolution of Ni dopant from the parent SFMNi perovskite surface is simulated by decreasing the dimensionless interaction energies from 4.5 to 2.5 at the 3×10^5th time step.

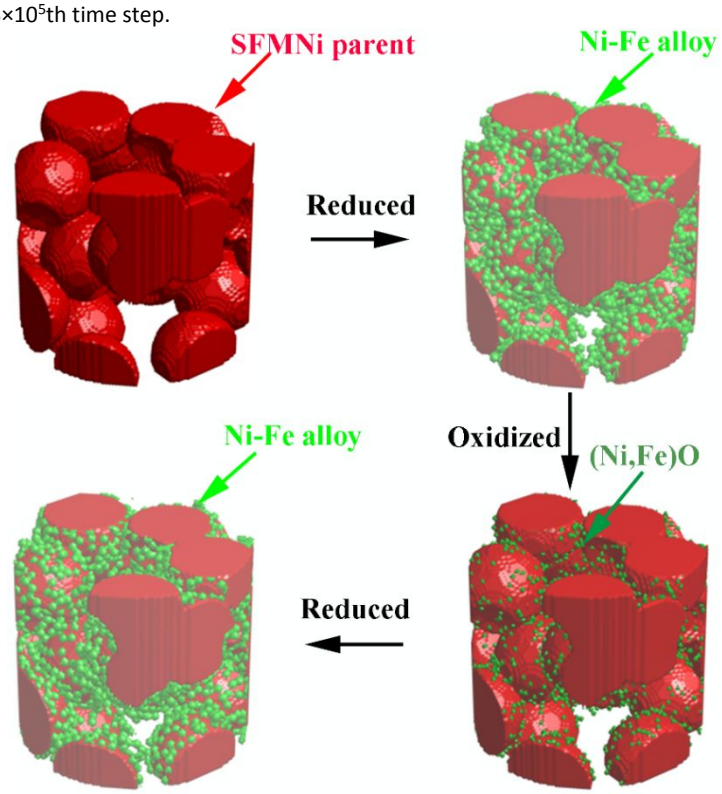

Scheme 1. Self-regeneration mechanism for SFMNi based materials with respect to the operating condition.

3.3. Electrochemical Performance

To further confirm the redox tolerance and self-regeneration of SFMNi based electrode, symmetrical cells with the cell configuration of SFMNi/LDC/LSGM/LDC/SFMNi, are measured in 13 redox cycles, performed by switching the atmosphere from air to N_2, then to 9.7%H_2-3%H_2O-87.3%N_2 and vice versa. Impedance spectra are measured in both the oxidizing and reducing atmosphere during each cycle, and the impedance spectra recorded at the 1st circle, 4th circle, 9th circle and 13th circle are shown in Figure 4a-b. In addition, the impedance spectra are also fitted by an equivalent circuit described as LR(QR)(QR), and the fitted electrode polarization resistance (R_p) at 800 °C as a function of the number of redox cycles is presented in Figure 4c. The initial R_p in the 9.7%H_2-3%H_2O-87.3%N_2 condition is measured and fitted to be 1.93 Ωcm^2, which is much higher than 0.57 Ωcm^2 measured in air, possibly because the p-type conductor SFMNi material has a much lower electrical conductivity in the reducing atmosphere compared to that in the oxidizing atmosphere. As shown in Figure S16 that when the gas is shifted from air to 9.7%H_2-3%H_2O-87.3%N_2, the electrical conductivities of the SFMNi sample are lowered at

400-800 °C, and the value recorded at 800 °C is decreased from 26.00 to 16.09 Scm^{-1}, which are in agreement with those predicted by the defect chemical model and the previously reported results [41]. It is also found that R_p measured in air first increases with increasing the redox cycles, and the value shows an increase up to 37% from 0.57 to 0.78 Ωcm^2 after 4 redox cycles. The cell performance degradation in air could be explained by the fact that the exsolved transition metal nanoparticles have not completely reincorporated into perovskite lattice, but instead converted to metal oxide during the re-oxidation process. On the other hand, after 4 redox cycles, R_p measured in air becomes stable, possibly ascribed to the balance between the formation of cuneiform (Ni,Fe)O particles and reincorporation of Ni and Fe elements into the parent oxide. The effect of redox cycle on the cell performance is totally different in the reducing atmosphere, and the cell performance is able to regenerate at 800 °C after each subsequent exposure to 9.7%H_2-3%H_2O-87.3%N_2 atmosphere during the redox cycle. R_p measured in the 9.7%H_2-3%H_2O-87.3%N_2 atmosphere is almost unchanged at about 1.93 Ωcm^2 with the fluctuation less than 0.15 Ωcm^2 during the redox cycles, and no obvious loss of the cell performance is observed with increasing the number of redox cycles. These results indicate that the transition metal oxides formed due to re-oxidation of the reduced SFMNi sample would disintegrate and release metallic Ni-Fe nanoparticles, leading to a complete self-regeneration of nano-structured electrode, further confirming that SFMNi-based material is a very promising alternative electrode for highly stable SOC application.

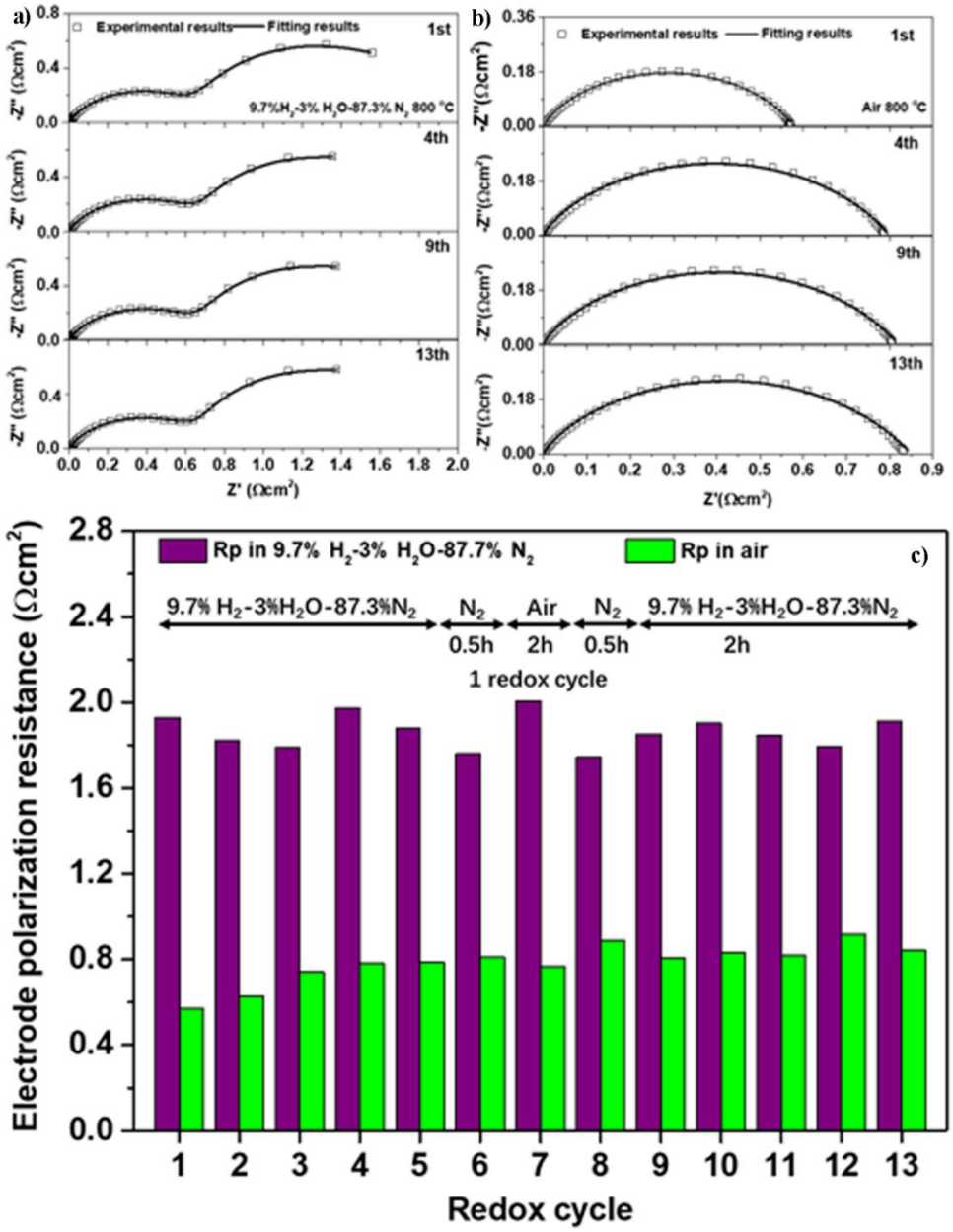

Figure 4 The electrode polarization resistance as a function of the number of redox cycles at 800 °C by switching the atmosphere from air to N_2 then 9.7%H_2-3%H_2O-87.3%N_2 and vice versa.

Redox cycling stability of the SFMNi-based composite cathode is also examined using single cells with cell configuration of SFMNi-SDC/LDC/LSGM/GDC-LSCF, and the morphology of the electrolyzer is shown in Figure S17. The electrolyzer is initially operated in a galvanostatic condition of -300 $mAcm^{-2}$ in 24%H_2O-76%H_2 atmosphere at 800 °C for 50 hours, showing a very stable cell voltage. The current load is then removed and the cell performance is evaluated to obtain the initial electrolysis current density and polarization resistance using *i-V* curves and impedance spectra characterization. Subsequently, the SFMNi composite cathode is subjected to redox cycle by switching the atmosphere from 24%H_2O-76%H_2 to air and vice versa using N_2 as the purging gas. Open circuit voltages (OCVs) are recorded until they become stable to make sure the atmosphere has been completely changed before the electrochemical performance test. The SFMNi based composite cathode is subjected to a total of 5 redox cycles, and the *i-V* curves as well as the impedance spectra have been displayed in Figure 5 and Figure S18-19. Figure 5a shows the *i-V* curves of SFMNi-SDC/LDC/LSGM/GDC-LSCF single cells measured at the 1st redox cycling. When comparing with the results measured at other redox cycles shown in Figure S18, it is found that no obvious change in the *i-V* curves is observed, and an electrolysis current density of -376, -400, -379, -374, and -373 $mAcm^{-2}$ is obtained at the 1st, 2nd, 3rd, 4th and 5th redox cycle under the cell voltage of 1.3 V (Figure 5b), respectively. With increasing the electrolysis cell voltage to 1.5V, the corresponding electrolysis current density increased to -653, -675, -653, -646, and -647 $mAcm^{-2}$, respectively, which are all much higher than that of SFM without Ni doping on the B-site and other ceramic cathode, and comparable to the state-of-the-art Ni cermet cathode, indicating that SFMNi materials are suitable for high-performance SOC application[11, 37, 46-51]. Furthermore, it is noted that redox cycling does not have detrimental effect on the SFMNi composite cathode due to its good self-regenerative capability, probably because the transition metals can change the states between the B-sites of the perovskite/metal oxide and metallic nanoparticles at different environment. Impedance spectra measured under OCV condition are also displayed (Figure 5c and Figure S19). As shown in Figure 5c, the cell total polarization resistance is measured to be 1.035, 1.035, 1.034, 1.036 and 1.042 Ωcm^2, respectively. Meanwhile, the electrode polarization resistance, corresponding to the intercept between high and low frequency at *x*-axis, is calculated to be 0.598, 0.596, 0.588, 0.589 and 0.589 Ωcm^2, respectively. It is obviously shown that both the total resistance and electrode polarization resistance do not change significantly during the 5-redox-cycle operation (Figure 5d), which is consistent with the result of no significant degradation of electrolysis current density in *i-V* curves (Figure 5b).

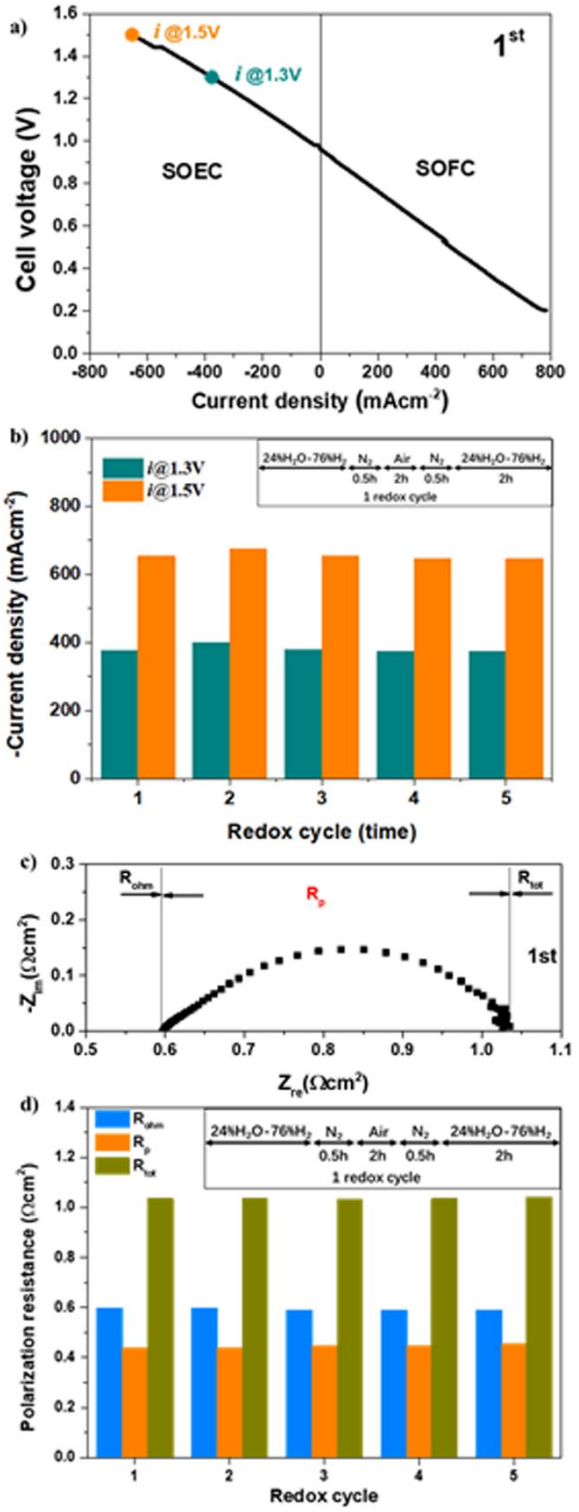

Figure 5 Redox cycling stability of the Ni-Fe@SFMNi nanostructured cathode in single cells with the configuration of SFMNi-SDC/LDC/LSGM/SDC-LSCF for steam electrolysis process, a) *i-V* curve at 1st cycle, b) electrolysis current densities at the applied electrolysis cell voltages of 1.3V and 1.5V as a function of the redox cycle, c) EIS curve at 1st cycle, and d) polarization resistance recorded at OCV condition as a function of the redox cycle.

Consequently, the XRD, XPS, SEM, TEM and electrochemical performance results have demonstrated that SFMNi material is

a very promising cathode for steam electrolysis application due to the impressive electrochemical performance and robust redox cycling stability via self-regeneration during the redox operation, showing a great potential to effectively accelerate the commercialization of the SOEC technology.

4. Conclusions

Ni doped to the B-site of the SFM parent perovskite oxide, SFMNi, has been evaluated as potential hydrogen electrode in solid oxide cells. Redox reversibility of the *in-situ* exsolved Fe-Ni nanoparticles are examined by the phase characterization and morphology observation during the redox cycling. XRD, SEM, and TEM results show that the reincorporation process of the exsolved Fe-Ni particles is not complete at 800 ^{o}C in air, and certain amount of Fe-Ni nanoparticles have been oxidized to transition metal oxides (Ni,Fe)O instead of reincorporation to the parent SFMNi perovskite oxide. However, the intermediate (Ni,Fe)O state presents no adverse effect on the self-regeneration process in the subsequent reduction treatment, and the electrode polarization resistance measured in air first increases but then maintains nearly stable after recovering in the 97%H_2-3%H_2O atmosphere. Solid oxide electrolyzer with Ni-Fe alloy nanoparticles decorated SFMNi cathode shows a robust redox cycling stability in the steam electrolysis process with a relatively stable electrolysis current density and polarization resistance during the exposure of the SFMNi-SDC cathode to 5 redox cycles.

Conflicts of interest

There are no conflicts to declare.

Acknowledgements

This work was supported by National Natural Science Foundation of China (51602228, 51502207, 21673062, 51402066), Natural Science Foundation of Jiangsu Province of China (BK20160380), Natural Science Foundation of Hubei Province of China (2016CFB243, 2017CFB655), the China Postdoctoral Science Foundation (2016M590712, 2017T100575) and the U.S. National Science Foundation (DMR–1832809).

Statement of Contributions

Y. W. and Y. Z. conceived and supervised the project. T. L. synthesized the materials, fabricated the cells, and performed electrochemical performance. Y. Z, X. Z, H. Z, W. Z., J. G. And F. C. conducted the XRD, XPS, SEM and TEM-EDS tests and analysis. G. J.and Y. Z. performed the modeling results. M. Y. Conducted the electrical conductivity test. All the authors (T. L., Y. Z., X. Z, H. Z, G. J., W. Z., J. G., F. C., M. Y., Y. Z., and Y. W.) wrote the manuscript.

Notes and references

‡ Footnotes relating to the main text should appear here. These might include comments relevant to but not central to the matter under discussion, limited experimental and spectral data, and crystallographic data.

§

§§

etc.

1 E. D. Wachsman, K. T. Lee, *Science,* 2011, **334**, 935-939.
2 Y. F. Song, W. Wang, L. Ge, X. M. Xu, Z. B. Zhang, P. Sergio, B. Juliao, W. Zhou, Z. P. Shao, *Adv. Sci.,* 2017, **4**, 1700337.
3 L. Bi, S. Boulfrad, E. Traversa, *Chem. Soc. Rev.,* 2014, **43,** 8255-8270.
4 W. Wu, H. P. Ding, Y. Y. Zhang, Y. Ding, P. Katiyar, P. K. Majumdar, T. He, D. Ding, *Adv. Sci.,* 2018, **5**, 1800360.
5 Y. Zheng, J. C. Wang, B. Yu, W. Q. Zhang, J. Chen, J. L. Qiao, J. J. Zhang, *Chem. Soc. Rev.,* 2017, **46**, 1427-1463.
6 R. C. Maher, P. R. Shearing, E. Brightman, D. J. L. Brett, N. P. Brandon, L. F. Cohen, *Adv. Sci.,* 2016, **3***,* 1500146.
7 A. J. Jacobson, *Chem. Mater.,* 2010, **22**, 660-674.
8 Y. Xia, Z. Jin, H. Wang, Z. Gong, H. Lv, R. Peng, W. Liu, L. Bi, *J. Mater. Chem. A*, 2019, **7**, 16136-16148.
9 A.J. Majewski, A. Dhir, *Mater. Renew. Sustain. Energy*, 2018, **7**, 16.
10 J. C. Ruiz-Morales, J. Canales-Vazquez, C. Savaniu, D. Marrero-Lopez, W. Z. Zhou, J. T. S. Irvine, *Nature,* 2006, **439**, 568-571.
11 W. Wang, C. Su, Y. Z. Wu, R. Ran, Z. P. Shao, *Chem. Rev.,* 2013, **113**, 8104-8151.
12 D. Sarantaridis, R. J. Chater, A. Atkinson, *J. Electrochem. Soc.,* 2008, **155**, B467-B472.
13 S. D. Kim, H. Moon, S. H. Hyun, J. Moon, J. Kim, H. W. Lee, *Solid State Ionics,* 2006, **177**, 931-938.
14 D. Sarantaridis, A. Atkinson, *Fuel Cells,* 2007, **7**, 246-258.
15 D. Neagu, G. Tsekouras, D.N. Miller, H. Menard, J.T. Irvine, *Nat. Chem*., 2013, **5**, 916-923.
16 D. Neagu, T.-S. Oh, D.N. Miller, H. Ménard, S.M. Bukhari, S.R. Gamble, R.J. Gorte, J.M. Vohs, J.T.S. Irvine, *Nat. Commun*., 2015, **6**, 8120.
17 Z. Du, H. Zhao, S. Yi, Q. Xia, Y. Gong, Y. Zhang, X. Cheng, Y. Li, L. Gu, K. Swierczek, *ACS Nano*, 2016, **10**, 8660-8669.
18 T. Zhu, H. E. Troiani, L. V. Mogni, M. Han, S. A. Barnett, *Joule,* 2018, **2**, 478-496.
19 J. Li, Y. Yu, Y.-M. Yin, N. Zhou, Z.-F. Ma, *Electrochim. Acta,* 2017, **235**, 317-322.
20 C. Yang, Z. Yang, C. Jin, G. Xiao, F. Chen, M. Han, *Adv. Mater.,* 2012, **24**, 1439-1443.
21 L. Ye, M. Zhang, P. Huang, G. Guo, M. Hong, C. Li, J. T. Irvine, K. Xie, *Nat. Commun.,* 2017, **8**, 14785.
22 J.-h. Myung, D. Neagu, D. N. Miller, J. T. S. Irvine, *Nature,* 2016, **537**, 528-531.
23 L. Z. Gan, L. T. Ye, C. Ruan, S. G. Chen, K. Xie, *Adv Sci.,* 2016, **3**, 1500186.
24 Y.F. Sun, Y.Q. Zhang, J. Chen, J.H. Li, Y.T. Zhu, Y.M. Zeng, B.S. Amirkhiz, J. Li, B. Hua, J.L. Luo, *Nano Lett.,* 2016, **16**, 5303-5309.
25 S. Liu, Q. Liu, X.-Z. Fu, J.-L. Luo, *Appl. Catal. B-Environ.,* 2018, **220***,* 283-289.
26 Y. Gao, D. Chen, M. Saccoccio, Z. Lu, F. Ciucci, *Nano Energ*., 2016, **27**, 499-508.
27 T.S. Oh, E.K. Rahani, D. Neagu, J.T. Irvine, V.B. Shenoy, R.J. Gorte, J.M. Vohs, *J. Phys. Chem. Lett.,* 2015, **6**, 5106-5110.
28 K.-Y. Lai, A. Manthiram, *Chem. Mater.,* 2018, **30**, 2838-2847.
29 K.-Y. Lai, A. Manthiram, *Chem. Mater.,* 2018, **30**, 2515-2525.
30 Y. Tian, L. Zhang, Y. Liu, L. Jia, J. Yang, B. Chi, J. Pu, J. Li, *J. Mater. Chem. A,* 2019, **7**, 6395-6400.
31 P. Steiger, D. Burnat, H. Madi, A. Mai, L. Holzer, J. V. Herle, O. Kröcher, A. Heel, D. Ferri, *Chem. Mater.*, 2019, **31**, 748-758.

32 P. Steiger, R. Delmelle, D. Foppiano, L. Holzer, A. Heel, M. Nachtegaal, O. Kröcher, D. Ferri, *ChemSusChem*, 2017, **10**, 2505-2517.
33 P. Steiger, M. Nachtegaal, O. Kröcher, D. Ferri, *ChemCatChem*, 2018, **10**, 4456-4464.
34 G. Yang, W. Zhou, M. Liu, Z. Shao, *ACS Appl. Mater. Interfaces,* 2016, **8**, 35308-35314.
35 K. Zhu, T. Wu, M. Li, R. Lu, X. Zhu, W. Yang, *J. Mater. Chem. A,* 2017, **5**, 19836-19845.
36 Y. Li, B. Hu, C. Xia, W.Q. Xu, J.P. Lemmon, F. Chen, *J. Mater. Chem. A*, 2017, **5**, 20833-20842.
37 Y. Wang, T. Liu, M. Li, C. Xia, B. Zhou, F. Chen, *J. Mater. Chem. A*, 2016, **4**,14163-14169.
38 Y. Wang, X. Lei, Y. Zhang, F. Chen, T. Liu, *J. Power Sources,* 2018, **405**, 114-123.
39 H. Lv, L. Lin, X. Zhang, D. Gao, Y. Song, Y. Zhou, Q. Liu, G. Wang, X. Bao, *J. Mater. Chem. A,* 2019*,* **7***,* 11967-11975*.*
40 G. Xiao, S. Wang, Y. Lin, Z. Yang, M. Han, F. Chen, *J. Electrochem. Soc.,* 2014, **161**, F305-F310.
41 N. Dai, J. Feng, Z. Wang, T. Jiang, W. Sun, J. Qiao, K. Sun, *J. Mater. Chem. A,* 2013, **1**, 14147-14153.
42 Y. Wang, T. Liu, S. Fang, F. Chen, *J. Power Sources,* 2016, **305**, 240-248.
43 Q. Liu, X. H. Dong, G. L. Xiao, F. Zhao, F. L. Chen, *Adv. Mater.,* 2010, **22**, 5478-5482.
44 Y. H. Li, Y. Li, Y. H. Wan, Y. Xie, J. F. Zhu, H. B. Pan, X. S. Zheng, C. R. Xia, *Adv. Energy Mater.,* 2019, **9**, 1803156.
45 G. Jiang, F. Yan, S. Wan, Z. Yanxiang, M. Yan, *Phys. Chem. Chem. Phys.,* 2019, **21**, 10902-10907.
46 C. Jin, C. Yang, F. Zhao, D. Cui, F. Chen, *Int. J. Hydrogen Energy,* 2011, **36**, 3340-3346.
47 Q. Liu, C. Yang, X. Dong, F. Chen, *Int. J. Hydrogen Energy*, 2010, **35**, 10039-10044.
48 G. Tsekouras, D. Neagu, J.T.S. Irvine, *Energy Environ. Sci.*, 2013, **6**, 256-266.
49 R. Xing, Y. Wang, Y. Zhu, S. Liu, C. Jin, *J. Power Sources,* 2015, **274**, 260-264.
50 T. Liu, Y. Wang, Y. Zhang, S. Fang, L. Lei, C. Ren, F. Chen, *Electrochem. Commun.,* 2015, **61**, 106-109.
51 C. Yang, Z. Yang, C. Jin, M. Liu, F. Chen, *Int. J. Hydrogen Energy.* 2013, **38**, 11202-11208.

Table of Contents Entry

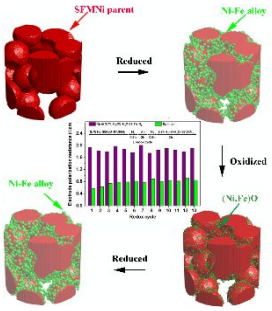

Herein, the redox-reversible stability of perovskite type SFMNi cathode decorated with *in-situ* exsolved Ni-Fe alloy nanoparticles is investigated by experimental results and explained by the exsolution-redissolution model.

.